PHYSICAL REVIEW B **71**, 075115 (2005)

Temperature dependence of the crystal structure and charge ordering in Yb_4As_3

U. Staub,[1] M. Shi,[1] C. Schulze-Briese,[1] B. D. Patterson,[1] F. Fauth,[2] E. Dooryhee,[3] L. Soderholm,[4] J. O. Cross,[5]
D. Mannix,[6] and A. Ochiai[7]
[1]*Swiss Light Source, Paul Scherrer Institut, CH-5232 Villigen PSI, Switzerland*
[2]*European Synchrotron Radiation Facility, F-38043 Grenoble Cedex, France*
[3]*Laboratoire de Cristallographie, CNRS, F-38042 Grenoble, France*
[4]*Chemistry Division, Argonne National Laboratory, Argonne, Illinois-60439, USA*
[5]*PNC-CAT, Advanced Photon Source, Argonne National Laboratory, Argonne, Illinois 60439, USA*
[6]*European Synchrotron Radiation Facility, BP220, F-38043 Grenoble Cedex, France*
[7]*Center for Low Temperature Science, Tohoku University, Sendai, 980-8578, Japan*

(Received 29 March 2004; revised manuscript received 24 November 2004; published 22 February 2005)

Resonant and nonresonant x-ray scattering, combined with x-ray absorption data, are presented on Yb_4As_3. The nonresonant data allow a detailed determination of the low-temperature crystal structure and its evolution as a function of temperature. Bond-valence-sum calculations are performed and compared with theoretical predictions. Using the structural knowledge, the energy dependence, near the Yb L_3 edge, of particular x-ray reflections are calculated and compared with experiment, and the temperature dependence of the charge order is extracted. A united picture of the temperature-dependent crystal structure and charge ordering in Yb_4As_3 emerges and is compared with theory.

DOI: 10.1103/PhysRevB.71.075115 PACS number(s): 71.30.+h, 64.60.−i, 61.10.Nz, 71.28.+d

I. INTRODUCTION

Electronic charge localization, leading to metal-insulator (MI) phase transitions, has attracted great interest, particularly in perovskites. It is associated with the disappearance of superconductivity in $La_{2-x}Sr_xCuO_4$ at particular Sr concentrations where charge stripes are formed,[1] and colossal magnetoresistance in the manganates occurs in connection with such a transition.[2] Although generally associated with transition metal oxides, charge localization also occurs in other materials.[3] A particularly interesting case is Yb_4As_3, where charge localization leads to a first-order charge-order transition[4] at $T_{CO}=290$ K. The resistivity above T_{CO} shows metallic behavior, exhibits a large discontinuity at T_{CO} and increases with decreasing temperature below this temperature. It then exhibits a maximum near 150 K, before decreasing again at still lower temperatures.[4] These effects have been ascribed to a temperature-dependent overlap in the narrow pnictide *p*-valence bands.[5] On the other hand, a strong enhancement of the linear term in the specific heat and a T^2 dependence in the low-temperature resistivity point to the occurrence of a Kondo effect. However, the very low carrier density in Yb_4As_3, 0.1% holes per formula unit,[4] indicates a different origin for these phenomena, because the charge carriers are required to screen the localized *f* states for the Kondo effect.

Charge-ordering leads to a structural phase transition in Yb_4As_3 from cubic ($I\bar{4}3d$) at room temperature to trigonal $R3c$ symmetry below T_{CO} and to two different Yb sites, occupied by the Yb^{2+} and Yb^{3+} ions, respectively. In the past, this structural phase transition and the associated temperature-dependent rhombohedral distortion from the cubic phase have been described[6] in terms of a cubic distortion angle $90+\alpha$. At room temperature, simple chemical considerations assuming As^{3-} for an ionic material lead to an intermediate Yb valence of 2.25. Theoretical calculations based on a single-hole band model predict[7] a slightly smaller Yb valence of 2.17, which are both in agreement with the results from Mössbauer spectroscopy[8] of 2.20 ± 0.05. Charge order below 290 K was first inferred from susceptibility measurements,[4] by Mössbauer experiments[8] and perturbed angular correlation measurements,[9] and finally confirmed by polarized neutron-scattering experiments.[10]

The polarized neutron-scattering experiments detected magnetic moments associated with the Yb^{3+} ions (Yb^{2+}, with a closed *f* shell, does not carry a magnetic moment), located on the body diagonal of the cube.[11] This study found unequal magnetic-field-induced moments at the two Yb sites, demonstrating that the charge ordering is incomplete even at very low temperatures. These moments were found to form a one-dimensional chain, and inelastic neutron-scattering results confirmed the one dimensionality of the magnetic interactions.[12–14]

Theoretical descriptions[15–17] based on the band Jahn-Teller effect describe the electronic properties of Yb_4As_3 and predict the temperature dependence of the charge-order parameter. Recently, resonant x-ray scattering experiments were performed,[18,19] that more directly confirmed the charge ordering and determined the charge-order parameter. The latter deviates significantly from the theoretical description and appears to be inconsistent with the temperature-dependent crystal structure. In view of these disagreements, it is important to compare the temperature dependence of the charge order with that of the crystal structure and with theoretical models.

A review of the magnetic and electronic properties of Yb_4As_3 can be found in Ref. 20. It is particularly interesting that this material is a good representative of a one-dimensional Heisenberg chain, for which the application of an external magnetic field opens a gap in the magnetic excitation spectrum.[21] The gap opening has been described in

1098-0121/2005/71(7)/075115(11)/$23.00

several theoretical studies,[22–27] some of which emphasize the particular local symmetry of the Yb^{3+} ions along the chain.

Again, a detailed knowledge of the structural parameters, as well as the degree of charge ordering, is important for understanding the magnetic properties. In this work, we present a detailed investigation of Yb_4As_3, performed with high-resolution powder diffraction, x-ray absorption spectroscopy on a powder sample, and resonant scattering on both a crystal and on polycrystalline material. Using high-resolution x-ray powder diffraction, the temperature dependence of the interatomic positions has been obtained. These have been used to calculate bond lengths and bond valence sums, from which a temperature dependence of the charge ordering is obtained. These results are compared with resonant x-ray scattering data, which can more directly determine the charge-order parameter, and with theory. The precise structural data obtained from this study and the x-ray absorption results have also been used to model the energy dependence of the resonant x-ray scattering data and to elucidate the strengths and limitations of the resonant x-ray scattering technique. A small amount of preliminary data has been published in Ref. 13.

II. EXPERIMENT

Single crystals were prepared as in Ref. 4. Resonant and nonresonant x-ray powder diffraction experiments were performed at BM16, at the ESRF, Grenoble (F). For the nonresonant diffraction experiments, the sample was filled in a 300 μm capillary, whereas for the resonant diffraction experiment, flat plate geometry was used. In both cases, a He-flow cryostat reached temperatures between 4.2 and 300 K, and a Ge-crystal analyzer crystal yielded high resolution. The nonresonant diffraction patterns were obtained with a photon energy of 34 972.4(3) eV ($\lambda=0.354\,52$ Å), calibrated using Si powder. The high energy was chosen to match sample transmission and capillary diameter. The resonant diffraction patterns were collected from 8900 to 9000 eV, around the Yb L_3 edge (8944 eV).

The x-ray absorption experiment was performed at BM1 at the ESRF. For this purpose, a small piece of crystal was ground in an inert atmosphere and mounted in a multifunctional "Lytle" detector,[28] allowing simultaneous measurements of x-ray transmission, fluorescence, and electron yield. These experiments were performed at room temperature.

The resonant scattering experiments on a single crystal of Yb_4As_3 were performed at beamline BM28 at the ESRF. For these experiments (111)-facets (cubic phase) were cut on a single crystal, $\sim 5\times 5\times 5$ mm^3, and a uniaxial stress was applied along [111] using a steel clamp, to obtain a single-domain sample in the charge-ordered phase. The clamped sample was mounted in a closed-cycle refrigerator, and thermal contact was achieved with Cu grease. A LiF (400) crystal reflection was used to analyze the polarization of the scattered radiation, in order to distinguish between the scattering from the $\sigma-\sigma$ and from the $\sigma-\pi$ chanel.

A. Crystal structure: Nonresonant powder diffraction

In cubic symmetry $I\bar{4}3d$, there is one distinct Yb and one distinct As site.[29] The Yb site is at the position 16(c), with one free coordinate x, and the As at 12(a), with no free coordinates. From our powder diffraction pattern taken at 300 K, we determine the lattice constant to be $a=8.791\,42(3)$ Å, and we obtain $x=0.0682(1)$. The Yb ions can be thought of as lying on 1d-chains, running parallel to the four body diagonals.

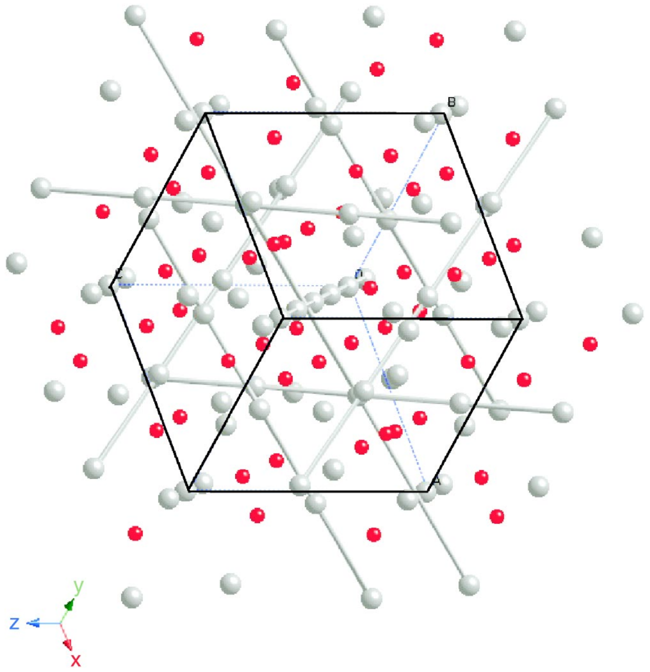

FIG. 1. (Color online) Crystal structure of Yb_4As_3 in the trigonal $R3c$ phase (rhombohedral settings). The Yb ions are connected to visualize the four different chains.

Below 290 K, the charge-ordering transition T_{CO}, the structure becomes trigonal $R3c$, with two inequivalent sites, Yb(1): 6(a) with one free coordinate z, and Yb(2): 18(b) with three free coordinates x, y, and z. The As has a single position 18(b), with three free coordinates x, y, and z. Here we used hexagonal (H_{ex}) settings as in most parts of the manuscript. Figure 1 however, is in cubic [rhombohedral (Rh)] settings. Note that the [111](Rh) corresponds to [001](H_{ex}). The Yb chains are now also of two types: one "short" chain [Yb(1)] (which goes through the center of the rhombohedron in Fig. 1), and three "long" chains [Yb(2)]. The holes are predominantly localized at Yb(1). Values of the temperature-dependent structural parameters, refined with the FULLPROF code,[30] are listed in Table I. A refinement to the diffraction pattern taken at $T=180$ K is shown in Fig. 2.

The temperature dependence of the (hexagonal) lattice constants are shown in Fig. 3. Whereas at low temperatures, both a and c increase continuously with increasing temperature, above 250 K, the lattice constant a turns over and decreases again, while c increases more steeply. The result is an approximately linear increase of the unit cell volume from 50 to 280 K (see Fig. 4). The temperature dependence of the lattice constants have been investigated previously[6] in the rhombohedral setting, with $a=b=c=a$(Rh) and a distorted-cube angle of $(90+\alpha)$. The rhombohedral and hexagonal lattice constants are related by

TABLE I. Refined structural parameters at different temperatures of Yb_4As_3 in the $R3c$ symmetry (hexagonal settings) and reliability indices obtained from Rietfeld refinements of the diffraction patterns. Yb(1) z has been fixed to its "cubic" value. Because the z values for all ions are free parameters, this choice defines the zero point of the z axis.

	20 K	50 K	120 K	150 K	200 K	220 K	240 K	260 K	280 K
a (Å)	12.483 36(3)	12.485 7(3)	12.495 57 (3)	12.501 50(3)	12.506 91(3)	12.511 22(3)	12.513 05(4)	12.513 64(4)	12.511 27(4)
c (Å)	7.483 36 (2)	7.484 59(2)	7.489 8 (2)	7.493 26 (2)	7.497 83 (3)	7.502 05 (3)	7.505 87 (3)	7.510 95 (3)	7.518 98 (3)
Yb(1) z	**0.405 85**	**0.405 85**	**0.405 85**	**0.405 85**	**0.405 85**	**0.405 85**	**0.405 85**	**0.405 85**	**0.405 85**
Yb(1) B($Å^2$)	0.22 (3)	0.30 (2)	0.47 (2)	0.58 (3)	0.57 (3)	0.59 (3)	0.61 (3)	0.66 (3)	0.71 (3)
Yb(2) x	0.214 13 (7)	0.214 06(6)	0.214 05 (7)	0.214 10 (7)	0.214 04 (7)	0.213 97 (7)	0.213 86 (8)	0.213 76 (8)	0.213 79 (8)
Yb(2) y	0.924 40 (6)	0.924 25(6)	0.924 23 (6)	0.924 23 (7)	0.924 19 (6)	0.924 18 (6)	0.924 06 (7)	0.924 08 (3)	0.924 1 (7)
Yb(2) z	0.0563 (3)	0.0568 (2)	0.0566(3)	0.0568 (3)	0.0569 (3)	0.0571 (3)	0.0569 (3)	0.0569 (3)	0.0573 (3)
Yb(2) B($Å^2$)	0.27 (2)	0.35 (1)	0.48 (2)	0.62 (4)	0.60 (2)	0.64 (2)	0.71 (2)	0.75 (2)	0.81 (2)
As x	0.9605 (2)	0.9606 (2)	0.9607 (2)	0.9606 (2)	0.9605 (2)	0.9604 (2)	0.9605 (2)	0.9604 (3)	0.9608 (3)
As y	0.7986 (2)	0.7988 (2)	0.7989 (2)	0.7985 (3)	0.7987 (2)	0.7985 (2)	0.7985 (3)	0.7982 (3)	0.7982 (3)
As z	0.1850 (3)	0.1856 (3)	0.1849 (3)	0.1855 (3)	0.1855 (3)	0.1857 (3)	0.1855 (3)	0.1855 (3)	0.1855 (4)
As B($Å^2$)	0.42 (4)	0.44 (3)	0.52 (3)	0.70 (4)	0.66 (4)	0.69 (4)	0.70 (4)	0.77 (4)	0.87 (4)
χ^2	2.33	2.02	2.07	1.98	2.58	3.32	3.08	3.31	3.26
R_{wp} %	12.3	11.1	11.6	11.7	11.2	10.8	11.2	11.2	11.5

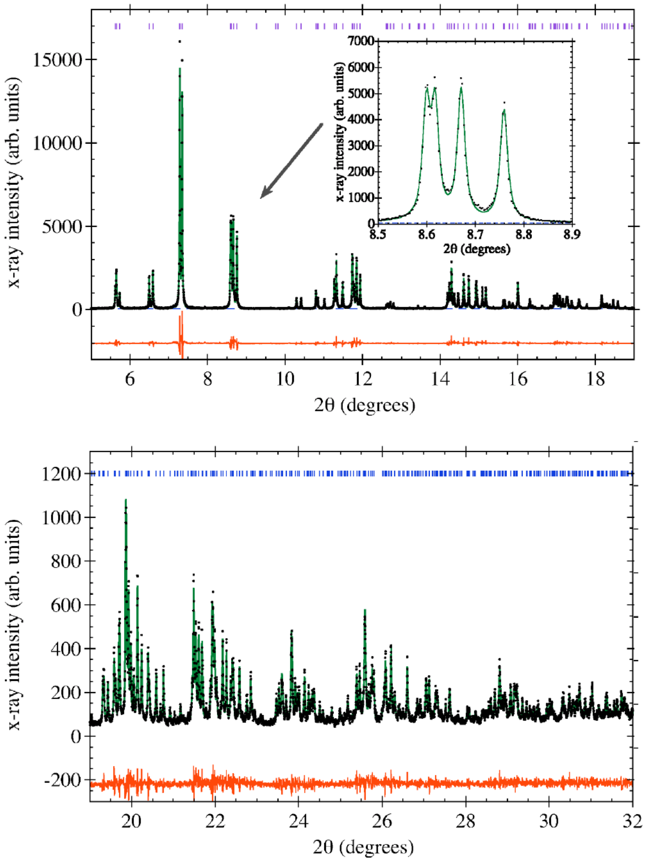

FIG. 2. Powder diffraction pattern (points) for Yb_4As_3 taken at $T=180$ K with refined fit (curve through the data), residuals (lower curve) and background (dashed curve) separated in two angular ranges. The inset shows an enlargement of the quartet investigated by resonant x-ray powder diffraction.

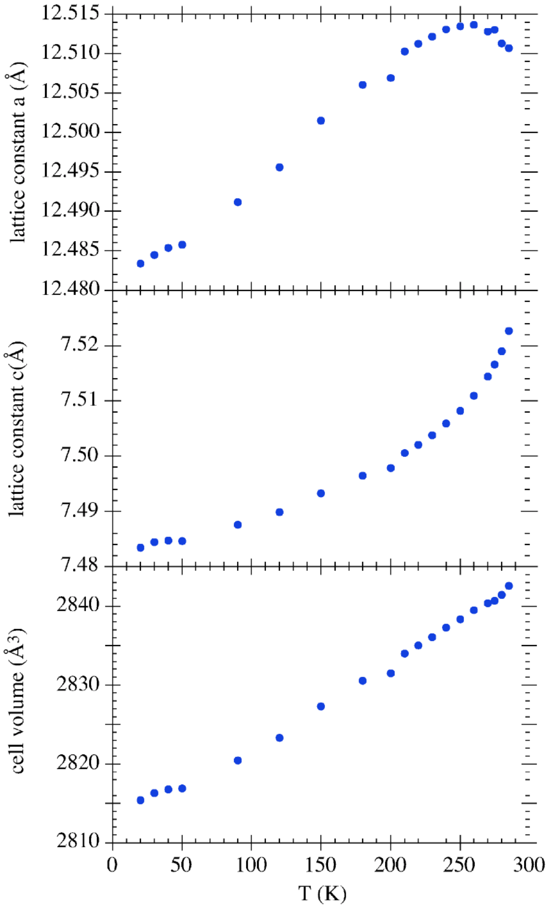

FIG. 3. Temperature dependence of the lattice constants a (top) and c (middle) and cell volume (bottom) (hexagonal setting) of Yb_4As_3.

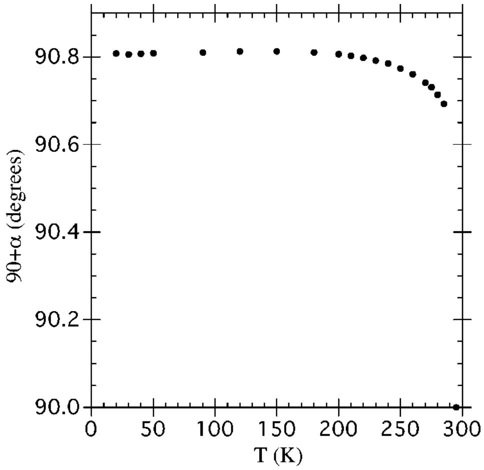

FIG. 4. Temperature dependence of the rhombohedral angle $90+\alpha$, reflecting the deviation from cubic symmetry.

$$a(\mathrm{Rh}) = \frac{a}{3}\sqrt{3 + \left(\frac{2c}{a}\right)^2}$$

$$\sin\alpha = \frac{\left(\frac{2c}{a}\right)^2 - \frac{3}{2}}{\left(\frac{2c}{a}\right)^2 + 3}.$$

However, the individual atomic coordinates have not previously been published, with the exception of a short communication[19] with our preliminary data for $T=200$ K. It should be noted that the distortion angle α, which is often used to relate structure and charge-ordering, neglects the important ionic displacements *within* the unit cell.

The local geometry of the short, Yb(1) chain is shown in Fig. 5. There is a threefold symmetry along this [111](Rh) direction, but no longer along the three other former body diagonals, reflecting the absence of Yb(2) site symmetry. The six As neighbors to Yb(1) form two identical triangles around the [111](Rh) axis, which at 20 K are rotated with respect to one another by 38.66°. This (temperature-dependent) rotation is an important structural characteristic which significantly affects the one-dimensional magnetic properties of the material.[23] It introduces a "phase shift" in the local bonding structure along the chain, which in turn is responsible, in an applied field, for the opening of a gap in the magnetic excitation spectrum.[21]

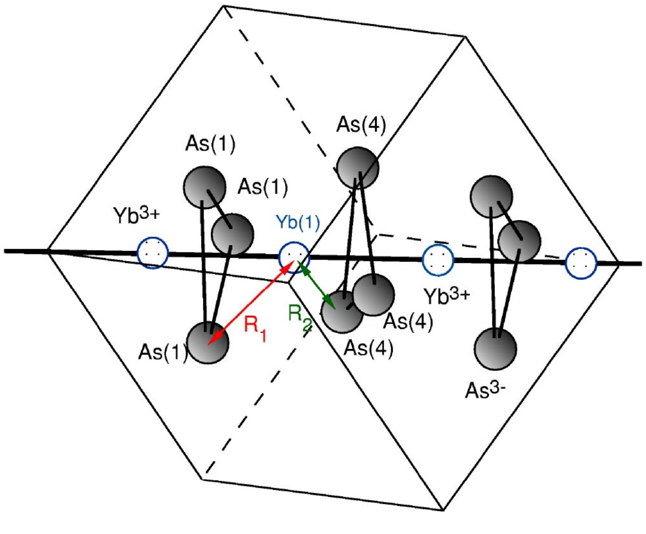

FIG. 5. Local crystal structure of the Yb^{3+} ions along the short chain, showing the various Yb–As distances.

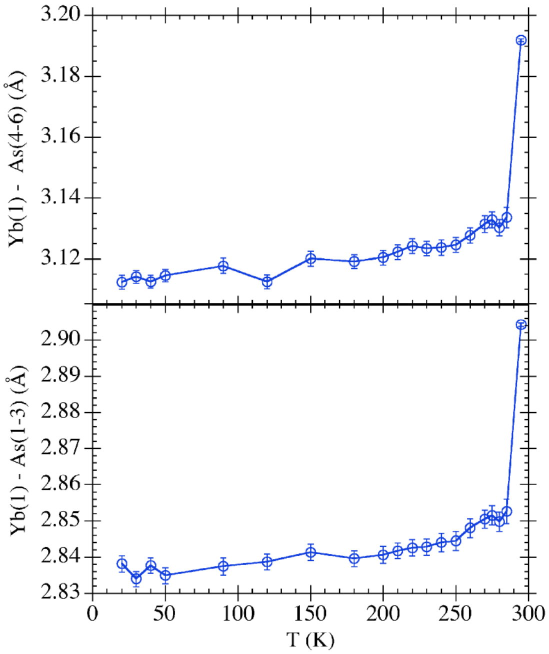

FIG. 6. The Yb(1)–As bond distances as a function of temperature. The lines are to guide the eye.

The temperature dependencies of the two inequivalent Yb(1)–As bond lengths are shown in Fig. 6. There are six inequivalent Yb(2)–As bond lengths, which again fall (roughly) into two triplets of uniform size: the shorter Yb(2)–As(1–3) bonds and the longer Yb(2)–As(4–6) bonds. The individual temperature dependencies are shown in Fig. 7. The average bond length of each Yb(2)–As–triplet is longer by 0.09 Å than the corresponding Yb(1)–As–triplet, indicating different ionic radii and hence different valence states for the Yb(1) and Yb(2) ions. The temperature dependencies of these bond lengths provide valuable information on the varying Yb valences. Aside from a slight increase in the bond distances due to thermal expansion, little change is seen in the shorter Yb(2)–As(1–3) distances. With increasing temperature above 240 K, the longer Yb(2)–As(4–6) distances tend to approach a single value, suddenly accomplishing this in the cubic phase above T_{CO}.

III. X-RAY ABSORPTION

Room temperature x-ray absorption near-edge structure (XANES) data for Yb_4As_3 are shown in the upper panel of Fig. 8, for the three types of measurement: fluorescence, transmission, and total electron yield, and the central panel shows a reference transmission measurement on Yb_2O_3. All

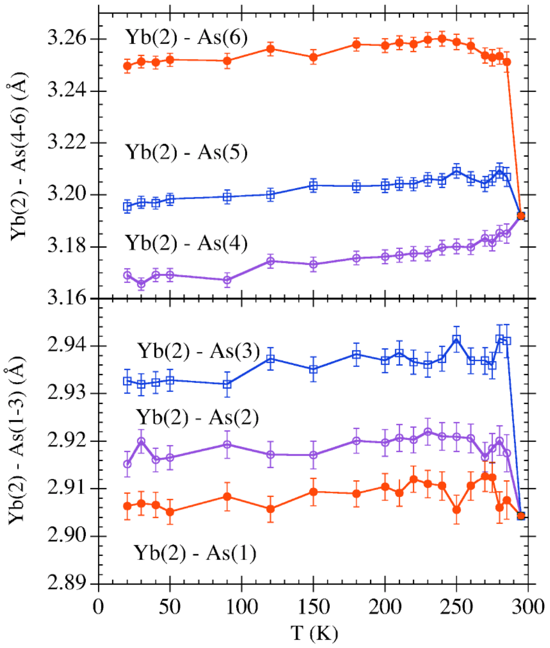

FIG. 7. (Color online) The Yb(2)–As bond distances as a function of temperature. The lines are to guide the eye.

three Yb_4As_3 curves exhibit a two-peak structure, with maxima located at ~8941 and 8948 eV, corresponding to dipole transitions from occupied 2*p*- to empty 5*d*-states for divalent and trivalent Yb, respectively.[31,32] The 7 eV separation is comparable to that seen with other divalent and trivalent rare-earth ions.[33] Note that the electron-yield data deviates from the other two techniques—a result of the high surface sensitivity of this technique and the likely presence of an oxidized layer with predominantly trivalent Yb. For the quantitative arguments below, the transmission data are used.

Following common procedures,[33] the XANES spectra were fitted using the sum of a Lorentzian and a step-like arctan function for each ionic contribution, Yb^{2+} and Yb^{3+} (lower panel in Fig. 8). In order to reduce the number of fitting parameters, the ratios of the Lorentzian and arctan amplitudes and widths were the same for both ions, and the energy separations of the Lorentzian and arctan functions were fixed to be equal. Finally, a convolution of the fit function with a Gaussian instrumental resolution function (FWHM: 2 eV) was included. The resulting Lorentzian width of the Yb^{2+} and Yb^{3+} ions, 9 eV, is significantly larger than the core-hole lifetime broadening,[34] 3.9 eV. The additional broadening could be an intrinsic effect, arising from hybridization in the metallic state, or simply due to distorted peak shapes caused by sample inhomogenities. The average Yb valence is given by the integrated Lorentzian intensities: $v = I_A/(I_A+I_B)+2$, resulting in 2.19(3) electrons, at $T = 295$ K. Note that the x-ray absorption process probes the timescale of the core hole life time broadening (3.9 eV $\approx 10^{-15}$ s) compared to the fluctuation time of the individual ion valences ($\sim 10^{-13}$ s), which is responsible for the observation of two absorption maxima and not a single resonance at an intermediate energy.

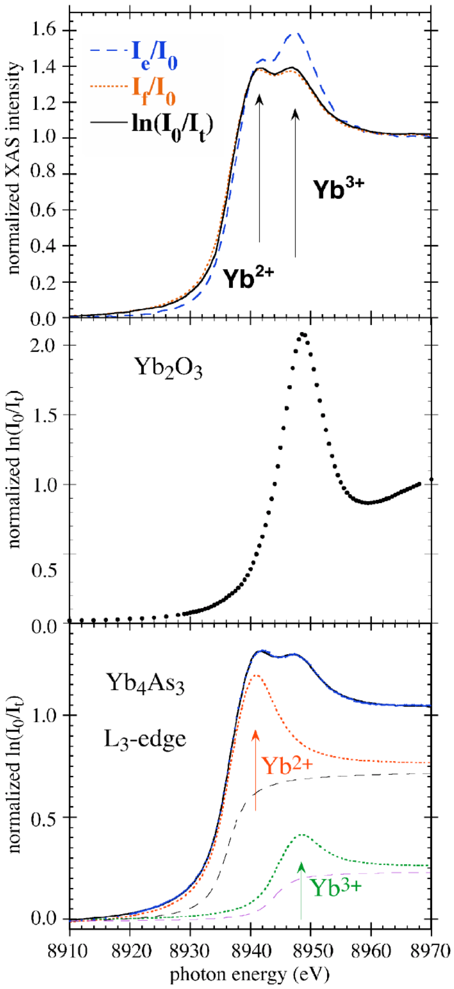

FIG. 8. (Color online) Top: x-ray absorption near-edge structure (XANES) at the Yb-L_3-edge of Yb_4As_3, taken with different detection modes (I_e: total electron yield, I_f: fluorescence yield, and I_t transmission) at room temperature. Middle: XANES of the trivalent standard Yb_2O_3. Bottom: Fit of the decomposition into a divalent and trivalent contribution (dotted curves). Broken lines reflect the arctan function.

IV. RESONANT POWDER DIFFRACTION

During the resonant powder diffraction experiments, full spectra were collected as a function of photon energy across the Yb L_3-absorption edge. The structure factor for a charge reflection can be written as

$$F_{hkl} = \sum_j f_j e^{i\mathbf{Q}\mathbf{R}_j} \delta(\mathbf{Q} - \tau_{hkl}), \qquad (1)$$

where $\mathbf{Q}$ is the x-ray momentum transfer, τ_{hkl} is the reciprocal lattice vector with Miller indices h,k,l, $\mathbf{R}_j$ is the position of ion j in the unit cell, and f_j is the corresponding atomic scattering factor. The scattering factor can in turn be decomposed as follows:

$$f_j(Q,E) = f_j^0(Q) + f_j'(E) + i f_j''(E), \qquad (2)$$

where $f_j^0(Q)$ is the x-ray atomic form factor, and $f_j'(E)$ and $f_j''(E)$ are the real and imaginary parts of the anomalous cor-

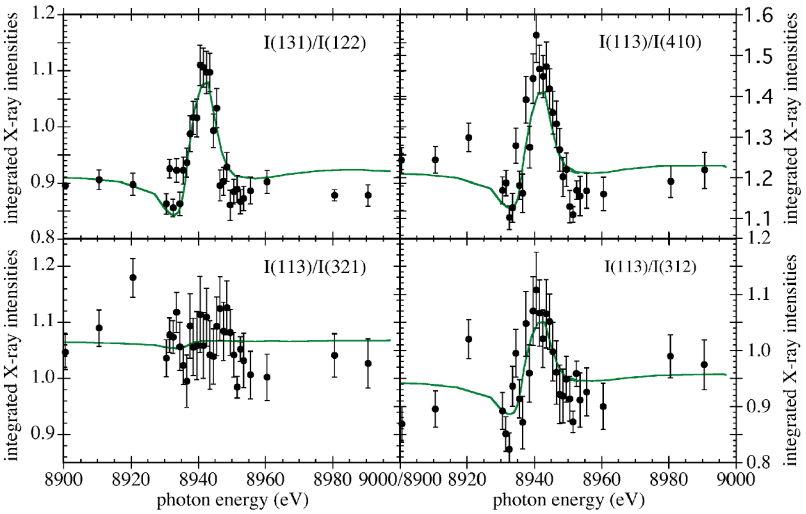

FIG. 9. Energy dependence of the ratios of integrated intensities of x-ray reflections taken with resonant powder diffraction at $T=200$ K.

rection factor. The quantities $f_j'(E)$ and $f_j''(E)$ contain the same physical information about the resonant ion, being related to one another by the Kramers-Kronig relation:

$$f_j'(E) = \frac{1}{\pi} P \int_{-\infty}^{\infty} \frac{f_j''(E')}{E' - E} dE' .$$

In this work, we take $f_j'(E)$ and $f_j''(E)$ to be scalar quantities. Because of the ionic character of the Yb ions, the contribution from the asphericity is expected to be weak compared to "pure" charge-ordering effects, which will affect even the strongest charge reflections. This is in contrast to the transition metal oxides, where the 3d-electrons participate in bonding, leading to strong overlap of orbitals and to large signals due to asphericity.[35–39] Furthermore, the powder diffraction experiment involves an average over all azimuthal orientations. A reliable description of the energy-dependent charge reflections therefore requires accurate knowledge of the real and imaginary parts of the Yb-scattering factors and of the correction due to absorption of the incoming and outgoing rays. It is generally true that the absorption correction for strongly absorbing polycrystalline samples is rather difficult to determine.

For the particular charge-ordering scheme of Yb_4As_3, the contributions to the total scattering of the Yb^{3+} (1) and Yb^{2+} (2) sites differ significantly for different strong charge reflections. Moreover, the strong cubic reflections are split into pairs or quartets in the rhombohedral symmetry (inset of Fig. 2). These splittings allow us to bypass the large absorption correction by considering only ratios of pairs or quartets of reflections, which are very closely spaced in 2θ. At the same time, this procedure automatically corrects for the detector efficiency. The energy dependence of selected ratios of reflections taken at $T=100$ K are shown in Fig. 9. The reflections (131) and (122) correspond to a particularly strong pair; the other reflections shown arise from a quartet at higher 2θ values. The integrated intensities were obtained by fitting the reflections to Voigt functions. A clear resonance is observed for the ratios $(131)/(122)$, $(113)/(410)$, and $(113)/(312)$, but the ratio $(113)/(321)$ shows little or no energy dependence.

To describe the energy dependence of these ratios, first we extracted the $f''(E)$, which are proportional to the respective absorption coefficients, from the individual Yb^{2+} and Yb^{3+} contributions to the XANES data (Fig. 8). With the use of the Kramers-Kronig transformation (using the program DIFFKK[40]), we obtained the real part of the scattering factor $f'(E)$ for Yb^{2+} and Yb^{3+}. These were used, together with the refined crystal structure data, as input to the program FULLPROF to calculate the energy dependence of the diffraction pattern. However, these calculations did not reproduce the observed intensity ratios: the observed anomalies exceed those calculated by a factor of approximately two. We attribute this discrepancy to the large Lorentzian linewidth found in the absorption data, which we discussed earlier.

In order to interpret the resonant powder data, we therefore used the approach of calculating $f''(E)$ from first principles, using the FEFF7 code.[41,42] To simulate the one electron difference between the 3+ and 2+ oxidation states, we performed calculations for Yb and Lu, each with the corresponding set of six nearest As neighbors. The obtained $f''(E)$ were then rescaled in energy to obtain the 7 eV difference between the two Yb^{2+} and Yb^{3+} absorption edges, as experimentally observed. Here the tabulated form factors of As and Yb^{3+} and Yb^{2+} were used for Yb(1) and Yb(2), respectively. The resulting $f''(E)$ [and $f'(E)$ from the Kramers-Kronig relation] are shown in Fig. 10 and were again used to calculate the energy-dependent intensity ratios for the different reflections. These calculations provide a good description of the observations, with the exception of an energy-independent offset. This offset, which is about 10%, is likely due to deviations of tabulated form factors[43] from the actual values and to remaining inaccuracies of the structural model. Proximity to an absorption edge not only affects the intensities of reflections, it also influences the scattering line widths. The dependence of the linewidth on $f''(E)$ has been demonstrated for a multilayer reflection in the soft x-ray regime.[44] This effect arises from the fact that the momentum transfer $\mathbf{k}$ of the x-ray is no longer a real quantity, $\mathbf{k}=\mathbf{q}+i[\mu(E)/\sin(\theta)]$, in which the delta function of the Bragg condition in reciprocal space is replaced by a Lorentzian with a linewidth of $\Gamma=2\mu(E)/\sin(\theta)$. Therefore, the broadening reflects the lim-

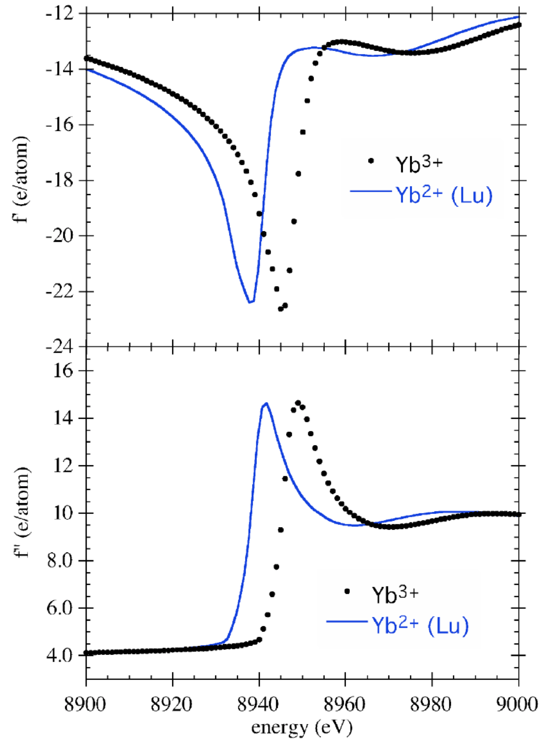

FIG. 10. (Color online) Energy dependence of the real $f'(E)$ and imaginary parts $f''(E)$ of the Yb^{2+} and Yb^{3+} scattering factors, from FEFF calculations. The Yb^{3+} scattering factors have been calculated for lutetium and rescaled in energy.

ited number of crystal planes sampled by the incoming x-rays, due to the energy-dependent absorption length. For a sufficiently well-crystallized sample and negligible instrumental resolution, we expect $\Gamma(E) \propto f''(E)$. Figure 11 shows the full width at half maximum (FWHM), averaged for the (113), (410), (321), and (312) reflections, compared with the scaled absorption data from the transmission measurement. The agreement is reasonable, and it demonstrates the importance of considering integrated intensities along all three dimensions in reciprocal space when performing energy-dependent x-ray diffraction on well-crystallized materials.

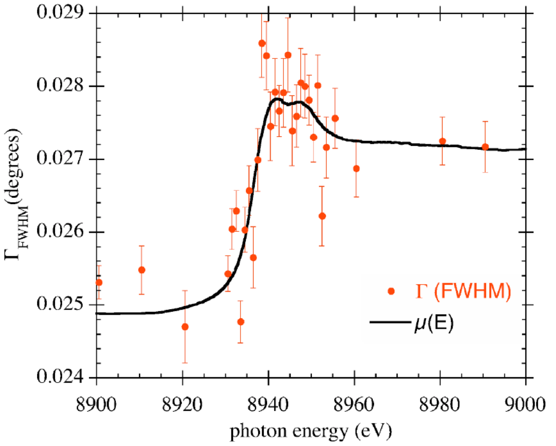

FIG. 11. Energy dependence of the average linewidth of particular reflections [(131), (122), (410), (321), and (312)] at $T=200$ K, compared with the rescaled XANES data [$\mu(E)$] taken in fluorescence mode.

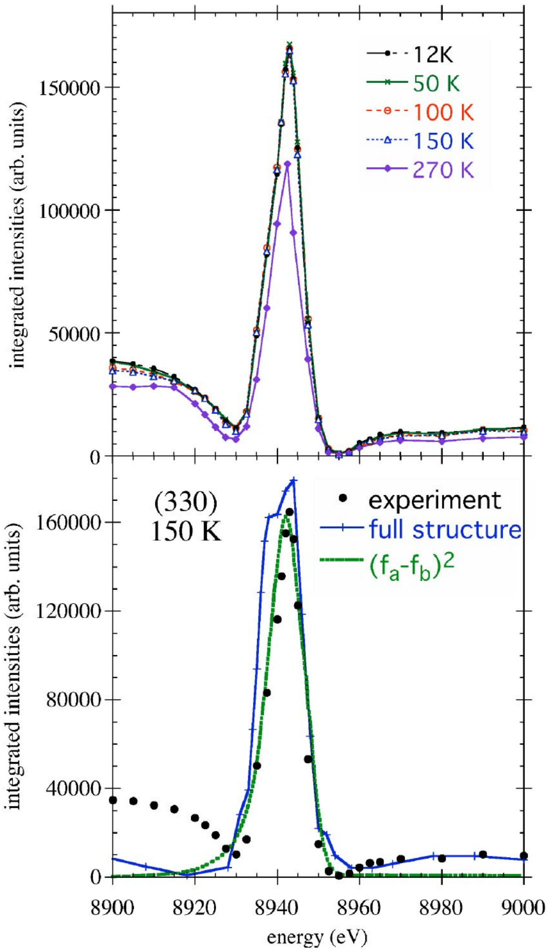

FIG. 12. (Color online) Energy dependence of the superlattice reflection (330) from the strained single crystal of Yb_4As_3, taken in the $(\tilde{\sigma}\sigma)$ polarization channel at different temperatures (Top): Here, the lines are guides to the eye. Energy dependence of the (330) reflection at 150 K, compared with a calculation based on the structural information obtained from the high-resolution powder diffraction and from the difference of the scattering factors $(f_a\text{-}f_b)^2$, where a and b stands for Yb^{2+} and Yb^{3+}, respectively.

V. RESONANT SCATTERING ON A SINGLE CRYSTAL

The energy dependence of the integrated (330) reflection is presented for different temperatures in Fig. 12. These data were collected using an analyzer crystal for polarization selectivity, and they correspond to unrotated light in the $\tilde{\sigma}\sigma$ channel. No intensity could be detected in the $\tilde{\sigma}\pi$ channel, in agreement with an isotropic charge distribution of the unoccupied states. The data show that at the maximum at 8941 eV, there is almost no temperature dependence between 12 and 150 K. The temperature dependence at lower energies, e.g., off-resonance at 8900 eV, is significantly larger. In a previous study,[18] the energy dependence of this reflection [note that cubic notation was used: $(3\,0\bar{3})$] was

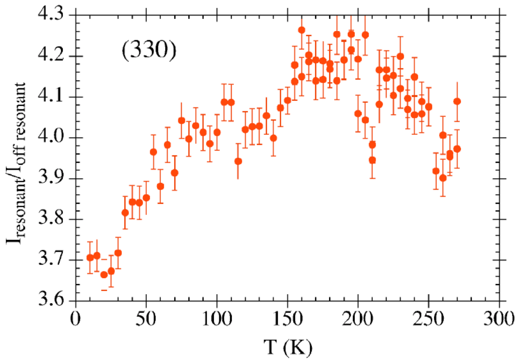

FIG. 13. Temperature dependence of the integrated intensity of the (330) reflection of Yb_4As_3, on- and off-resonance, taken with the strained crystal with $(\tilde{\sigma}\sigma)$ polarization.

described to be simply proportional to $(f_a\text{-}f_b)^2$, with f_a and f_b corresponding to the scattering factors of the Yb^{2+} and Yb^{3+} ions, respectively. Effects of ionic movement within the unit cell were neglected. Now, with the detailed crystal structures at hand, we can calculate the energy dependence of this reflection without this approximation, with the result included in Fig. 12. The data have been corrected for absorption. The qualitative agreement confirms that the intensity at resonance is still dominated by the difference $f_a\text{-}f_b$, as previously assumed. Note that there is no energy dependence if the scattering factors at the two sites are equal (charge disorder). However, off resonance, the observed intensity is significantly larger than predicted. The reason may be the same as for the off-resonance powder data, but the shape of the resonance is also different: the energy-dependent calculation shows a peak that is less sharp and more symmetric than observed. These deviations are likely caused by inaccurate first-principle calculations of the energy-dependent scattering factors; the calculations may overestimate the width of the white-line features in the imaginary parts of the scattering factors. A correction would lead to a narrower peak in the energy dependence and to an increased ratio between the on- and off-resonance intensities, as observed in the resonant powder experiment (see Fig. 9). However, it may also be affected by the inaccuracy of the structural model, which leads to much larger deviations for weak reflections than for the very strong ones.

To highlight the differences in the temperature-dependencies on- and off-resonance, temperature-dependent integrated intensities were collected at 8942 and 8900 eV. Figure 13 shows the temperature-dependent ratio between the resonant and nonresonant integrated intensities. First the ratio increases with increasing temperature before turning over near 180 K and decreasing again above 220 K. This temperature dependence is reminiscent of that of both the pseudocubic distortion angle α (Fig. 4) and the resistivity, and it reflects either the charge order more directly or the interatomic adjustments. One should note the possibility, as has been previously proposed,[45] that there exist *different* order parameters for the charge ordering and for the crystallographic distortions.

VI. DISCUSSION

An accurate description of the magnetic properties of Yb_4As_3 requires good knowledge of the $4f$ wave functions, which in turn are determined by the crystal-electric-field (CEF) interaction. The normal procedure to determine such wave functions is to begin with experimental inelastic neutron scattering[12] data and to construct a consistent $4f$-level splitting scheme. However, approximations have to be used, since the number of neutron observations is rather limited and the number of independent parameters is large, due to the low point symmetry (C_3) of the magnetic Yb^{3+} ions on site Yb(1). Model calculations[24] have been performed for the higher symmetry C_{3v}. But such an approximation is inappropriate, due to the significant deviation of the local structure from C_{3v}. Another study[46] simply neglects a higher-order parameter, but this leads to an important orientation ambiguity. A promising approach would be to use very accurate structural information to calculate the CEF parameters in a point-charge model, as has been successfully done[47] for high-T_c superconductors. This calculation, on $RBa_2Cu_3O_{7-\delta}$, demonstrates the accuracy with which the structural parameters must be known: changes much smaller than those occurring at the tetragonal-orthorhombic MI transition in $RBa_2Cu_3O_{7-\delta}$ significantly affect the CEF states. The detailed low-temperature structural information provided by this work could form the basis of such an analysis.

We now turn to the relationship in Yb_4As_3 between the crystal structure and charge order. The charge order is defined as the quantum mechanical expectation value, averaged over time and equivalent crystallographic sites, to find a given charge at the Yb ion. The electron, when there, is in a well localized f state. As we have shown, taking the charge-order parameter to be the difference $f_a\text{-}f_b$, the resonant intensity of the (330)-reflection is proportional to the order-parameter squared. However, such an approximation may not be *a priori* correct. In particular, for transition metal ions it has been argued that the resonant signal reflects a bond length change and not directly the orbital ordering.[48–50] These effects are also clearly visible in linear x-ray absorption experiments at the K edge of transition metal ions. For $4f$-electron materials, however, it is well known that different bond lengths and different species of anions in general have a smaller effect on the lanthanide L edges[33] compared to the large chemical shift (Yb of 7 eV). Resonant inelastic x-ray scattering experiments did not see any shift of the excitations energies under high pressure, even though the valence is changed and the lattice contractions is of order of 10% (e.g., Dallera *et al.*[51]). It is known that under applied pressure, which causes a much larger (10%) local distortion than the 0.02 Å (<1%) changes we see in Yb_4As_3, only very small changes are observed in the XANES (see Ref. 33). Another possibility to obtain the influence of bond distance changes on the anomalous scattering factors is the use of first principle calculations. Here we use the FEFF8[41,42] code to calculate the changes due to the bond distances on $f''(E)$ of the two Yb ions at 20 and 285 K (see Fig. 15). The temperature-dependent differences for both sites are less than 1% compared with the very large change of more than a factor of 2 induced by the 7 eV chemical shift. This further

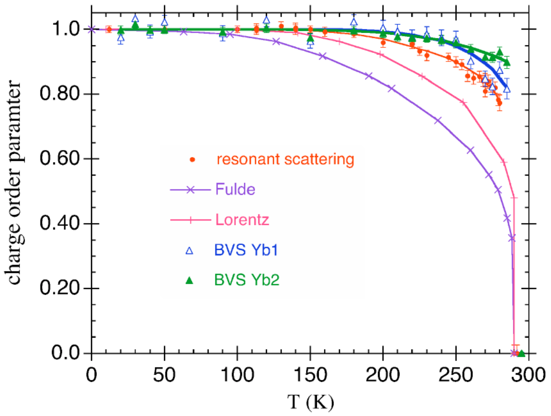

FIG. 14. (Color online) Charge-order parameter obtained from: the bond-valence-sums of Yb(1) and Yb(2) (triangles), the resonant x-ray scattering intensity (circles), the bond angle deviation from cubic α and the models of Fulde (Refs. 15 and 54).

supports the conclusion that although the bond distance changes indeed contribute to the change in scattering factors, and consequently in the resonant intensities, the contribution is expected to be neglible.

For these reasons, it can be concluded that the resonant signal is a reasonable measure of the charge-order parameter, represented here by f_a-f_b. We have shown that the temperature dependence of this parameter neither follows the theoretical prediction[15] nor does it simply scale with the distortion angle α, of the strucutre.[18] Figures 6 and 7 show that the temperature dependence of the bond lengths is weak below T_{CO}, compared to the jump seen at the transition, therefore the expected valence change is weak as well. A convenient way to correlate the bond-length changes with the valence changes is to calculate the "bond valence sum" (BVS), defined as

$$V_i = \sum_j \exp[(R_{ij} - d_{ij})/b],$$

with $b=0.37$ as the general parameter, R_{ij} as the bond length between the ith and jth ion and $d_{ij}=2.59$ Å[52,53] the parameter for the Yb—As bond, which gives the correct Yb^{3+} valences for Yb in YbAs. To correct for thermal expansion, we rescale the bond lengths with the cube root of the temperature-dependent cell volume. The obtained low temperatures value for Yb(1) and Yb(2) are 2.27 and 1.81, respectively, which deviate significantly from the expected 3+ and 2+ values. Finally, the temperature-dependent valence is obtained by scaling the corresponding BVS by the expected valence changes of $3-2.25=0.75\,e$ and $2.25-2=0.25\,e$, for the Yb(1) and Yb(2), respectively, between ambient and 20 K. The order parameters thus obtained are compared to the those from the resonant x-ray scattering measurement[18] and from theoretical models in Fig. 14. The order parameter from the BVS of Yb(2) is expected to be much more precise than for Yb(1), since the change in valence of Yb(1) from the cubic phase to low temperature is 0.75 e, compared to only 0.25 e for Yb(2). Both have a temperature dependence very similar to that of the angle α which lies between them and was also predicted in Ref. 17. The similarity between the results from the BVS with those of the distortion angle α and that the differences between the charge order parameter obtained from resonant scattering and that from the BVS is not likely due to atomic displacements within the unit cell. Both theoretical models clearly overestimate the temperature-dependent changes. Note that the model of Lorentz[54] is based on calculations for a very similar charge-order material, $\mathrm{Eu_4As_3}$. As noted previously, the differences seen between the structural order and the charge order may either be due to inaccuracies in the structural parameters or to the existence of separate order parameters.

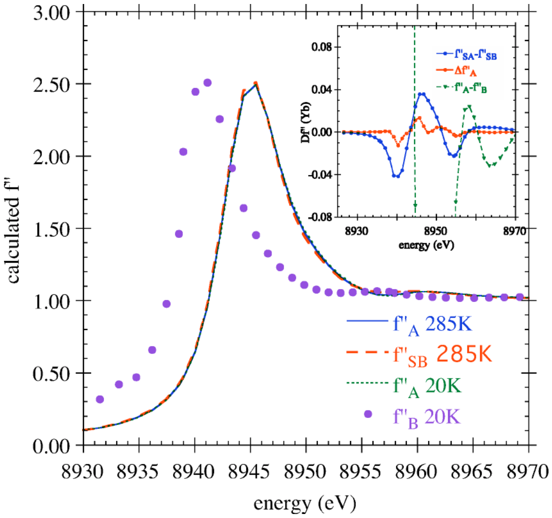

FIG. 15. (Color online) Calculated imaginary parts of the scattering factors considering only the influence of the bond valence changes using FEFF8. f''_A and f''_B reflect the scattering factors of the 2+ and 3+ of the Yb site A and B states, respectively, and f''_{SB} of the local structure of the Yb B site but with a 3+ state. The inset shows the differences of the imaginary part of the scattering factors in an enlarged scale showing that the effects due to changes of the local structure are insignificant.

Very recently, by comparison with $\mathrm{Sm_4Bi_3}$,[55] a different charge ordering scheme for $\mathrm{Yb_4As_3}$ has been proposed.[56] The scenario has been put forward that the Yb(2) is always in its divalent state below T_{CO} and the holes are grabbed from the As bands. This scenario would explain some of the discrepancies we have in the energy dependent calculation of the reflections. Moreover, it would not give any temperature dependence of the BVS calculations for Yb(2). Indeed, a much weaker dependence is observed for Yb(2) than expected from the change in valence of 0.25 compared with that of 0.75 expected for Yb(1). However, from the observed temperature dependence there is also a temperature dependence of the BVS for Yb(2), indicating that the system is best described by an intermediate scenario, in which some holes are acquired from the As bands and some are transferred from the Yb(2) to the Yb(1) site. This scenario would also be in good agreement with the valence of 2.19+ obtained from our XANES data, as this would indicate that below T_{CO}, the Yb(2) valence would approach Yb^{2+} before Yb(1) can reach its trivalent state.

VII. CONCLUSION

Our resonant and nonresonant x-ray diffraction study has provided detailed parameters for the low-temperature structure of Yb_4As_3. Our powder diffraction data demonstrate that the temperature-dependent structure, as evidenced by the bond-valence values, deviates from the charge-order parameter obtained from resonant x-ray scattering and from theory. These deviations could be caused by the different time scales of the charge and lattice fluctuations, leading to different order parameters. The differences between the order parameters could in principle also be caused by the influence of the bond distances on the scattering factors, although such a scenario is not supported by our calculations. The BVS results indicate further that the charge ordering is not simply a freezing out of the charge carriers hopping between Yb, but additionally the Yb(1) are acquiring holes from the As bands. We have demonstrated that a rather direct determination of the charge order can also be obtained from resonant powder diffraction. Moreover, we have found that the line width is energy dependent at the absorption edge, reflecting a strong contribution of the sampling depth to the observed line widths.

ACKNOWLEDGMENTS

The authors would like to acknowledge the technical assistance of the Swiss Norwegian Beamline Team (BM1 at the ESRF) during the x-ray absorption measurement. This work was supported by the Swiss National Science Foundation and (L.S.) the U.S. DOE, OBES, Chemical Sciences, under Contract No. W-31-109-ENG-38.

---

[1] J. M. Tranquada, B. J. Sternlieb, J. D. Axe, Y. Nakamura, and S. Uchida, Nature (London) **375**, 6532 (1995).

[2] R. M. Kusters, J. Singleton, D. A. Keon, R. M. Greedy, and W. Hayes, Physica B **155**, 362 (1989).

[3] P. G. Radaelli, Y. Horibe, M. J. Gutmann, H. Ishibashi, C. H. Chen, R. M. Ibberson, Y. Koyama, Y.-S. Hor, V. Kiryukhin, and S.-W. Cheong, Nature (London) **416**, 155 (2002).

[4] A. Ochiai, T. Suzuki, and T. Kasuya, J. Phys. Soc. Jpn. **59**, 4129 (1990).

[5] V. N. Antonov, A. N. Yaresko, A. Y. Perlov, P. Thalmeier, P. Fulde, P. M. Oppeneer, and H. Eschrig, Phys. Rev. B **58**, 9752 (1998).

[6] K. Iwasa, M. Kohgi, N. Nakajima, R. Yoshitake, Y. Hisazaki, H. Osumi, K. Tajima, N. Wakabayashi, Y. Haga, A. Ochiai, T. Suzuki, and A. Uesawa, J. Magn. Magn. Mater. **177–181**, 393 (1998).

[7] T. Kasuya, J. Phys. Soc. Jpn. **63**, 2481 (1994).

[8] P. Bonville, A. Ochiai, T. Suzuki, and E. Vincent, J. Phys. I **4**, 595 (1994).

[9] M. Rams, K. Królas, K. Tomala, A. Ochiai, and T. Suzuki, Hyperfine Interact. **97–98**, 125 (1996).

[10] M. Kohgi, K. Iwasa, A. Ochiai, T. Suzuki, J.-M. Mignot, B. Gillon, A. Guskasov, J. Schweizer, K. Kakurai, M. Nishi, A. Dönni, and T. Osakabe, Physica B **230–232**, 638 (1997).

[11] M. Kohgi, K. Iwasa, A. Ochiai, T. Suzuki, J.-M. Mignot, B. Gillon, A. Gukasov, J. Schweizer, K. Kakurai, M. Nishi, A. Dönni, and T. Osakabe, Physica B **230–232**, 638 (1997).

[12] M. Kohgi, K. Iwasa, J.-M. Mignot, A. Ochiai, and T. Suzuki, Phys. Rev. B **56**, R11 388 (1997).

[13] M. Kohgi, K. Iwasa, J. M. Mignot, B. Fak, P. Gegenwart, M. Lang, A. Ochiai, H. Aoki, and T. Suzuki, Phys. Rev. Lett. **86**, 2439 (2001).

[14] K. Iwasa, M. Kohgi, A. Gukasov, J. M. Mignot, N. Shibata, A. Ochiai, H. Aoki, and T. Suzuki, Phys. Rev. B **65**, 052408 (2002).

[15] P. Fulde, B. Schmidt, and P. Thalmeier, Europhys. Lett. **31**, 323 (1995).

[16] Y. M. Li, N. d'Ambrumenil, and P. Fulde, Phys. Rev. B **57**, R14 016 (1998).

[17] Y. M. Li, N. d'Ambrumenil, and P. Fulde, Phys. Rev. Lett. **78**, 3386 (1997).

[18] U. Staub, B. D. Patterson, C. Schulze-Briese, F. Fauth, M. Shi, L. Soderholm, G. B. M. Vaughan, and A. Ochiai, Europhys. Lett. **53**, 72 (2001).

[19] U. Staub, B. D. Patterson, C. Schulze-Birese, F. Fauth, M. Shi, L. Soderholm, G. B. M. Vaughan, E. Dooryhee, J. O. Crossa, and A. Ochiai, Physica B **318**, 284 (2002).

[20] B. Schmidt, H. Aoki, T. Cichorek, J. Custers, P. Gegenwart, M. Kohgi, M. Lang, C. Langhammer, A. Ochiai, S. Paschen, F. Steglich, T. Suzuki, P. Thalmeier, B. Wand, and A. Yaresko, Physica B **300**, 121 (2001).

[21] M. Köppen, M. Lang, R. Helfrich, F. Steglich, P. Thalmeier, B. Schmidt, B. Wand, D. Pankert, H. Benner, H. Aoki, and A. Ochiai, Phys. Rev. Lett. **82**, 4548 (1999).

[22] D. V. Dmitriev, V. Y. Krivnov, and A. A. Ovchinnikov, Phys. Rev. B **65**, 172409 (2002).

[23] H. Shiba, K. Ueda, and O. Sakai, J. Phys. Soc. Jpn. **69**, 1439 (2000).

[24] G. Uimin, Y. Kudasov, P. Fulde, and A. Ovchinnikaov, Eur. Phys. J. B **16**, 241 (2000).

[25] M. Oshikawa, K. Ueda, H. Aoki, A. Ochiai, and M. Kohgi, J. Phys. Soc. Jpn. **68**, 3181 (1999).

[26] A. A. Zvyagin, Phys. Rev. B **62**, 12 175 (2000).

[27] B. Schmidt, P. Thalmeier, and P. Fulde, Europhys. Lett. **35**, 109 (1996).

[28] F. W. Lytle, in *Applications of Synchrotron Radiation*, edited by H. Winick, D. Xian, M. H. Ye, and T. Huang (Gordon and Breach, New York, 1989), Vol. 4, p. 135.

[29] *International Tables for Crystallography* (D. Reidel, Dordrecht, 1983).

[30] J. Rodriguez-Carvajal, Physica B **192**, 55 (1993).

[31] K. Syassen, G. Wortmann, J. Feldhaus, K. H. Frank, and G. Kaindl, Phys. Rev. B **26**, 4745 (1982).

[32] I. Felner, I. Nowik, D. Vaknin, U. Potzel, J. Moser, G. M. Kalvius, G. Wortmann, G. Schmiester, G. Hilscher, E. Gratz, C. Schmitzer, N. Pillmayr, K. G. Prasad, H. d. Waard, and H. Pinto, Phys. Rev. B **35**, 6956 (1987).

[33] J. Röhler, in *Handbook on the Physics and Chemistry of Rare*

Earths, edited by K. A. Gschneidner, Jr., L. Eyring, and S. Hüfner (North-Holland, Amsterdam, 1987), Vol. 10, p. 453.

[34] M. O. Krause and J. H. Oliver, J. Phys. Chem. Ref. Data **8**, 329 (1979).

[35] D. H. Templeton and L. K. Templeton, Acta Crystallogr., Sect. A: Cryst. Phys., Diffr., Theor. Gen. Crystallogr. **36**, 237 (1980).

[36] Y. Murakami, J. P. Hill, D. Gibbs, M. Blume, I. Koyama, M. Tanaka, H. Kawata, T. Arima, Y. Tokura, K. Hirota, and Y. Endoh, Phys. Rev. Lett. **81**, 582 (1998).

[37] S. Grenier, A. Toader, J. E. Lorenzo, Y. Joly, B. Grenier, S. Ravy, L. P. Regnault, H. Renevier, J. Y. Henry, J. Jegoudez, and A. Revcolevschi, Phys. Rev. B **65**, 180101(R) (2002).

[38] H. Nakao, Y. Wakabayashi, T. Kiyama, Y. Murakami, M. V. Zimmermann, J. P. Hill, D. Gibbs, S. Ishihara, Y. Taguchi, and Y. Tokura, Phys. Rev. B **66**, 184419 (2002).

[39] S. Grenier, J. P. Hill, D. Gibbs, K. J. Thomas, M. v. Zimmermann, C. S. Nelson, V. Kiryukhin, Y. Tokura, Y. Tomioka, D. Casa, T. Gog, and C. Venkataraman, Phys. Rev. B **69**, 134419 (2004).

[40] http://cars.uchicagp.edu/∼newville/dafs/diffkk/.

[41] S. I. Zabinsky, J. J. Rehr, A. Ankudinov, R. C. Albers, and M. J. Eller, Phys. Rev. B **52**, 2995 (1995).

[42] J. J. Rehr, J. M. de Leon, S. I. Zabinsky, and R. C. Alberts, J. Am. Chem. Soc. **113**, 5136 (1991).

[43] E. N. Maslen, A. G. Fox, and M. A. O'Keefe, in *International Tables for Crystallography*, edited by A. J. C. Wilson and E. Prince (Kluwer Academic, Dordrecht, 1992), Vol. C, p. 548.

[44] L. Sève, J. M. Tonnerre, and D. Raoux, J. Appl. Crystallogr. **31**, 700 (1998).

[45] U. Staub, G. I. Meijer, F. Fauth, R. Allenspach, J. G. Bednorz, J. Karpinski, S. M. Kazakov, L. Paolasini, and F. d'Acapito, Phys. Rev. Lett. **88**, 126402 (2002).

[46] O. Sakai, M. Kohgi, H. Shiba, A. Ochiai, H. Aoki, K. Takegahara, and H. Harima, J. Phys. Soc. Jpn. **69**, 3633 (2001).

[47] U. Staub and L. Soderholm, in *Handbook on the Physics and Chemistry of Rare Earths*, edited by K. A. Gschneidner, Jr. and L. Eyring (North-Holland, Amsterdam, 2000), Vol. 30, p. 491.

[48] M. Benfatto, Y. Joly, and C. R. Natoli, Phys. Rev. Lett. **83**, 636 (1999).

[49] I. S. Elfimov, V. I. Anisimov, and G. A. Sawatzky, Phys. Rev. Lett. **82**, 4264 (1999).

[50] P. Benedetti, J. v. d. Brink, E. Pavarini, A. Vigliante, and P. Wochner, Phys. Rev. B **63**, 060408 (2001).

[51] C. Dallera, E. Annese, J. P. Rueff, A. Palenzona, G. Vankó, L. Braicovich, A. Shukla, and M. Grioni, Phys. Rev. B **68**, 245114 (2003).

[52] E. N. Brese and M. O'Keefe, Acta Cryst. B **47**, 192 (1991).

[53] I. D. Brown, *The Bond Valence Model* (Oxford University Press, New York, 2002).

[54] B. Lorenz, Phys. Stat. Sol. **125**, 375 (1984).

[55] S. Suga, A. Sekiyama, S. Imada, T. Suzuki, H. Aoki, and A. Ochiai, Physica B **281&282**, 158 (2000).

[56] M. Shirakawa, H. Aoki, and A. Ochiai, J. Phys. Soc. Jpn. **72**, 2893 (2003).